



**HAL**  
open science

# A discrete element thermo-mechanical modelling of diffuse damage induced by thermal expansion mismatch of two-phase materials

Damien André, Bertrand Levraut, Nicolas Tessier-Doyen, Marc Huger

## ► To cite this version:

Damien André, Bertrand Levraut, Nicolas Tessier-Doyen, Marc Huger. A discrete element thermo-mechanical modelling of diffuse damage induced by thermal expansion mismatch of two-phase materials. *Computer Methods in Applied Mechanics and Engineering*, 2017, 318, pp.898-916. 10.1016/j.cma.2017.01.029 . hal-01549675

**HAL Id: hal-01549675**

**<https://hal.science/hal-01549675>**

Submitted on 29 Jun 2017

**HAL** is a multi-disciplinary open access archive for the deposit and dissemination of scientific research documents, whether they are published or not. The documents may come from teaching and research institutions in France or abroad, or from public or private research centers.

L'archive ouverte pluridisciplinaire **HAL**, est destinée au dépôt et à la diffusion de documents scientifiques de niveau recherche, publiés ou non, émanant des établissements d'enseignement et de recherche français ou étrangers, des laboratoires publics ou privés.

# A discrete element thermo-mechanical modelling of diffuse damage induced by thermal expansion mismatch of two-phase materials

Damien André<sup>a,\*</sup>, Bertrand Levraut<sup>a</sup>, Nicolas Tessier-Doyen<sup>b</sup>, Marc Huger<sup>a</sup>

<sup>a</sup>*ENSCI, SPCTS, UMR 7315, F-87000 Limoges, France*

<sup>b</sup>*Univ. Limoges, SPCTS, UMR 7315, F-87000 Limoges, France.*

---

## Abstract

At the macroscopic scale, brittle media such as rocks, concretes or ceramics can be seen as homogeneous continua. However, at the microscopic scale, these materials involve sophisticated microstructures that mix several phases. Generally, these microstructures are composed of a large amount of inclusions embedded in a brittle matrix that ensures the cohesion of the material. These materials generally exhibit complex mechanical behaviors resulting from the interactions between the different phases of the microstructure.

As a result, the macroscopic behavior of these media may be predicted considering an accurate knowledge of their microstructures. This paper proposes a model to study the impact of diffuse damage resulting from thermal expansion mismatch between the mixed phases. This type of damage (which is not catastrophic for the integrity of two-phase materials) may appear when heterogeneous materials are subjected to thermal cycles.

This phenomenon involves a high amount of discontinuities and can not be tackled easily with the Finite Element Method (FEM). The Discrete Element Method (DEM) naturally accounts for discontinuities and is therefore a good alternative to the continuum approaches. However, the difficulty with DEM is to perform quantitative simulations because the mechanical quantities are not described in terms of the classical continuum theory. This study describes the approach used here to tackle this fundamental difficulty. The results given by the

---

\*Corresponding author

E-mail: damien.andre@unilim.fr

Tel: (33)/(0) 5 87 50 24 42

proposed approach are finally compared to experimental observations.

*Keywords:* discrete element method, DEM, thermal expansion, damages, silica, alumina, inclusion, brittle, crack, damage, Young's modulus

---

## 1. Introduction

Rocks, concretes or ceramics are heterogeneous materials exhibiting multi-phase compositions involving different sizes of aggregates, various bonding phases and additives. Description and prediction of thermo-mechanical behavior of such materials present a real difficulty due to their complex microstructure. Hashin & Shtrikman (H&S) have developed an analytic method to predict thermo-mechanical properties of perfectly cohesive (free of damage) multi-phase materials (1). However, most of these materials present numerous micro-cracks at room temperature. These micro-cracks result from thermal expansion mismatches between their different phases. These local defects highly influence thermo-mechanical properties and may have a great influence on materials lifetime in service conditions.

For instance, Young's modulus is strongly affected by the presence of micro-cracks and the measured values are often in disagreement with H&S's prediction (2, 3). The study proposed here focuses on a numerical method able to predict the occurrence of these defects and their overall influence on macroscopic properties such as Young's modulus and Coefficient of Thermal Expansion (CTE). Any materials that exhibit coarse aggregates such as concretes, rocks or ceramics may be addressed by the presented method.

Various numerical approaches can be distinguished. In the mechanical engineering field, the most used is the Finite Element Method (FEM). FEM, which is the most widespread technique is well suitable for materials characterized by reliable stress-strain laws. However, at the microscopic scale, this method is not adapted to describe discontinuities (4) without assumptions on their localization, their paths, their growths and their coalescences. Alternative methods to FEM exist such as X-FEM (Extended Finite Element Method) that keeps the rate of convergence towards singularities (micro-cracks) thanks to form functions. However, this method is adapted to describe the crack propagation in quasi-static mode but is not suitable for the management of opening and closure of numerous micro-cracks simultaneously.

The DEM is an interesting alternative way to study multi-damaged materials because it takes naturally into account discontinuities. The DEM implements a group of distinct elements (also named *discrete element*) which are in interaction

through contacts or cohesive laws. This model consists in an assembly of discrete elements, deformable or not, linked by simple mechanical laws. The advantage is the natural description of crack initiation, crack propagation and coalescence. Researchers have used this method to study damages in solids, such as concretes (5), rocks (6) or ceramics (7). However, the main difficulty is to get quantitative predictions. This is due to the necessity to find relations between microscopic laws, at the discrete element scale, and the macroscopic properties, at the structure scale. In this study the considered macroscopic properties are Young's modulus, Poisson's ratio, coefficient of thermal expansion and failure strength.

In this study, only the thermo-mechanical effects are taken into account. To avoid complex physico-chemical interactions, a model material is preferred in place of an industrial one. The phases of this model material have been chosen to ensure chemical neutrality and to avoid the presence of interphases. This model material is composed of two phases : spherical alumina inclusions embedded in a borosilicate glass matrix. The selected model material exhibits a positive CTE mismatch between the glass matrix and the alumina inclusions.

A short first section is dedicated to model material processing. The second section focuses on the H&S analytic model whose limits are highlighted. The third and fourth section introduces the DEM model. In this part, the method to model thermal expansion with DEM, that presents an innovative feature, is focused. As a preliminary validation, the next section proposes the implementation of the DEM model without cracks. The numerical results are compared to the H&S predictions. In the last part, the micro-cracks are implemented and the given numerical results are compared to the experimental data in terms of macroscopic Young's modulus and CTE. The capability of the presented method to simulate, understand and predict qualitatively and quantitatively the impact of the micro-crack density on thermo-mechanical properties is finally discussed.

## **2. Experimental study**

The material used for this work is a *model material*. A model material mimics, through a simplified framework, a given decoupled phenomenon observed with real and complex materials. In order to study the impact of thermal expansion mismatches, a two-phase model material, composed of mono-diameter spherical alumina inclusion embedded in a borosilicate glass matrix, is preferred. The thermo-mechanical parameters values for alumina and glass were chosen to produce a micro-crack network during the cooling stage of the sample preparation.

<b>Properties</b>	<b>Matrix</b>	<b>Inclusion</b>
Material	Glass	Alumina
Expansion coefficient $\alpha_{[50-450^{\circ}C]}(K^{-1})$	$11.6 \times 10^{-6}$	$7.6 \times 10^{-6}$
Young modulus E (GPa)	72	340
Poisson ratio $\nu$	0.23	0.24
Bulk density $\rho$ ( $kg.m^{-3}$ )	2570	3970
Tensile stress limit (MPa)	50	380

Table 1: Matrix and inclusions thermo-mechanical properties

### 2.1. Processing of two-phase model materials

The model materials used in this study are composed of spherical monomodal alumina inclusions (average diameter equals to  $500 \mu m$ ) which are randomly placed in a borosilicate glass matrix. Alumina (corundum phase) is a single oxide-based ceramic exhibiting fine grains. The main requirements of the selected glass matrix are homogeneity, isotropy, a rather chemical inertia and the capability to monitor thermal expansion coefficient. In this way, a borosilicate glass has been prepared from the melting of a vitrifiable mixture initially constituted by different raw materials containing silica, boron oxide and other secondary oxides. After grinding and sieving at  $40 \mu m$ , the glass powder was mixed during 3 hours with a slight proportion of organic additives used as binder and lubricant. A perfectly controlled volume fraction of alumina inclusions is incorporated in the mixture and is homogenized during 1 hour to ensure the dispersion of spherical alumina inclusions. Green specimens ( $80 \times 40 \times 10 mm^3$ ) are shaped by uni-axial pressing (80 MPa) before debinding and sintering under uni-axial pressure (15MPa at  $600^{\circ}C$ ) to remove residual porosity. Three different volume fractions of inclusion were prepared (15%, 30% and 45%). Figure 1 shows the microstructure of a final two-phase model material highlighting the crack network.

### 2.2. Induced residual thermal stresses

The thermo-mechanical properties of both individual materials are given in Table 1. The selected model material exhibits a thermal expansion mismatch such as :

$$\Delta\alpha = \alpha_{matrix} - \alpha_{inclusion}, \text{ with } \Delta\alpha = 4 \times 10^{-6} K^{-1} \text{ so } \Delta\alpha > 0 \quad (1)$$

The introduction of spherical particles in a matrix, which are chemically and physically different, leads the occurring of thermal stresses during the cooling

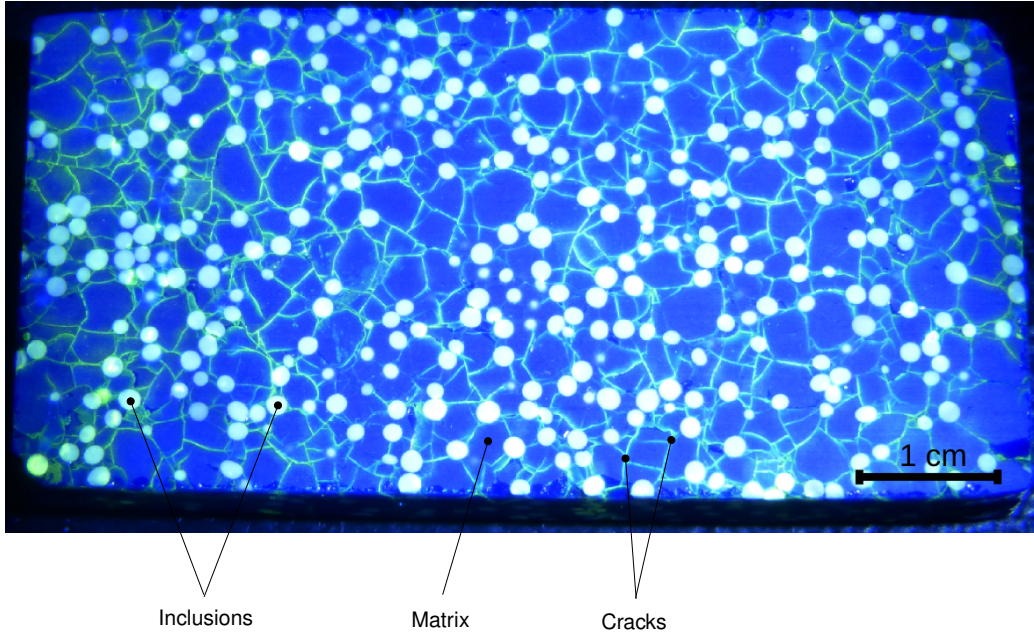


Figure 1: Microstructure of a generated cracking network

stage of the sample processing. Because of the positive CTE mismatch, the matrix is under tensile mode and the inclusions are subjected to compressive stresses. Figure 2 describes this phenomenon for a single inclusion. The matrix is subjected to  $\sigma_{\text{orth}}$  and  $\sigma_{\text{rad}}$ . The brittleness of the glass matrix induces orthoradial cracks that occur and propagate in the matrix. In the case of a unique inclusion, the radial and orthoradial stresses  $\sigma_{\text{rad}}$  and  $\sigma_{\text{orth}}$  can be deduced from the hydrostatic pressure  $p$  at the interface (8):

$$p = (\alpha_m - \alpha_p) \Delta T \left( \frac{1 + \nu_m}{2E_m} + \frac{1 - 2\nu_p}{E_p} \right)^{-1} \quad (2)$$

with :

$$\sigma_{\text{rad}} = -p \quad \text{and} \quad \sigma_{\text{orth}} = \frac{p}{2} \quad (3)$$

with :

- 'm' and 'p' indices are respectively the matrix and the inclusion,
- $\alpha_i$  is the CTE and

- $E_i$  and  $\nu_i$  are respectively the Young's modulus and the Poisson's ratio.

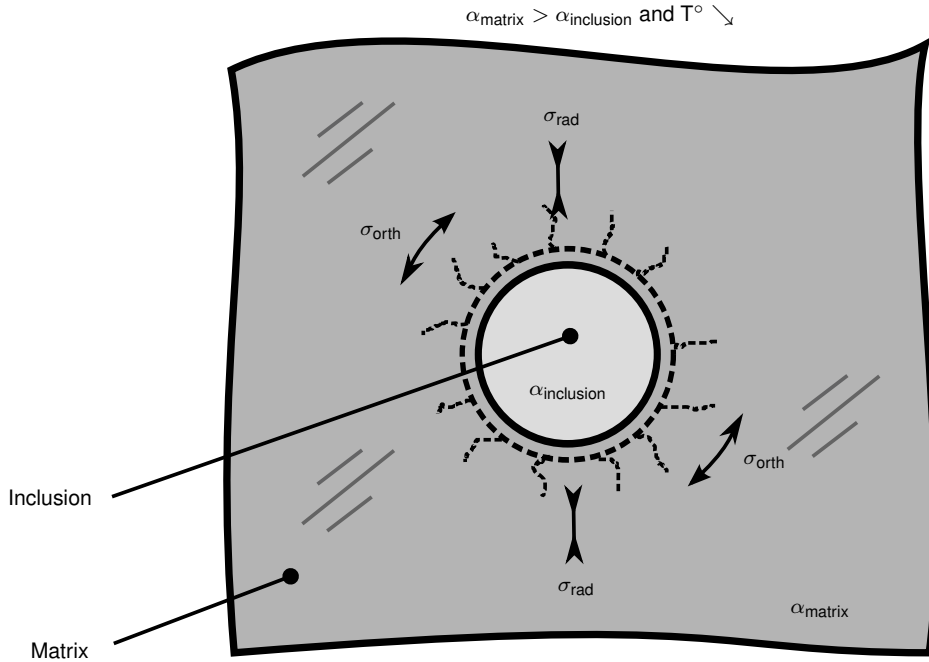


Figure 2: Sketch of the residual stresses and induced damages during cooling stage

When multiple inclusions are present, a complex crack network is created. Figure 1 shows an example of this crack network.

### 3. The Hashin & Shtrikman model

Among the various theoretical approaches developed to predict elastic and thermal properties of two-phase materials, the H&S bounds are used here. This analytic approach seems well suited to describe inclusional materials (1). The apparent Young's modulus can be predicted from the knowledge of (i) both volume fractions of the matrix ( $v_m$ ) and inclusional particles ( $v_p$ ), (ii) bulk and shear modulus of each phase noted  $K_m$ ,  $G_m$ ,  $K_p$ , and  $G_p$  respectively. The bounds of the

apparent bulk modulus  $K_v^-$  and  $K_v^+$  are computed as :

$$K_v^- = K_m + \frac{v_p}{\frac{1}{K_p - K_m} + \frac{3v_m}{3K_m + 4G_m}} \quad (4)$$

$$K_v^+ = K_p + \frac{v_m}{\frac{1}{K_m - K_p} + \frac{3v_p}{3K_p + 4G_p}} \quad (5)$$

The bounds of the apparent shear modulus  $G_v^-$  and  $G_v^+$  are computed as :

$$G_v^- = G_m + \frac{v_p}{\frac{1}{G_p - G_m} + \frac{6(K_m + 2G_m)v_m}{5G_m(3K_m + 4G_m)}} \quad (6)$$

$$G_v^+ = G_p + \frac{v_m}{\frac{1}{G_m - G_p} + \frac{6(K_p + 2G_p)v_p}{5G_p(3K_p + 4G_p)}} \quad (7)$$

The bounds of apparent Young's modulus  $E_v^-$ ,  $E_v^+$  are computed as :

$$E_v^- = \frac{9K_v^- G_v^-}{3K_v^- + G_v^-} \quad (8)$$

$$E_v^+ = \frac{9K_v^+ G_v^+}{3K_v^+ + G_v^+} \quad (9)$$

As shown in Figure 3, the plots of the experimental Young's modulus and CTE are lower than H&S lower bound ( $HS^-$ ) prediction. The Young's modulus was measured through an ultrasonic technique and the CTE with a standard dilatometer equipment.

The presented results underline the impact of the micro-cracked microstructure on the macroscopic thermo-mechanical behavior. The micro-cracks lead to a significative loss of E and  $\alpha$  values compared to the H&S prediction. When the volume fraction of inclusions (15%, 30% and 45%) increases, the results for E values tend to enhance and for  $\alpha$  values, they tend to decrease.

The following parts of this paper will introduce the discrete element model used to predict apparent Young's modulus and apparent CTE that can not be treated with H&S models.

#### 4. The discrete element model

Thanks to the spectacular improvement of computer performances in the last two decades, DEM approach has met a growing interest in the scientific community. Many methods based on the original DEM proposed by Cundall and Strack

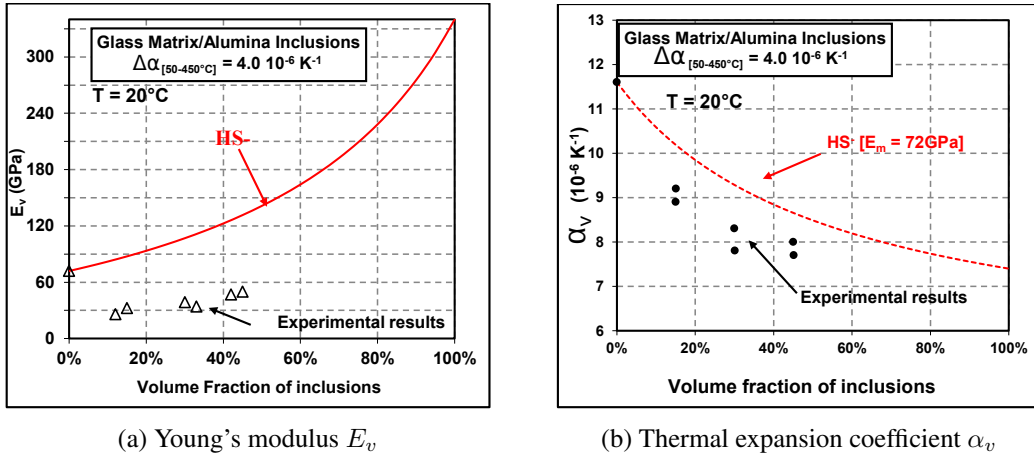


Figure 3: Comparison between experimental thermo-mechanical properties and analytic prediction at room temperature

(9) have been proposed in the literature. Among these methods, the *lattice* model allows to study a continuum as a set of simple physical interactions between discrete elements. For example, Schlangen in (10) proposed to study the fracture of concretes with discrete elements bonded by mechanical beams. With such a model, a major problem is that the discrete elements are material points without volume nor shape.

An interesting approach is to mix *lattice* and *particle* models as it was first proposed by Potyondy in (11). It has been widely used to study phenomena that cannot be treated with the Finite Element Methods (FEM) such as tribological problems with wear phenomena. Unlike continuous approaches, the main difficulty for DEM is to simulate quantitatively the continuum. The purpose of the free DEM software *GranOO*<sup>1</sup> is to face this difficulty. At this time, *GranOO* embeds models that allow quantitative simulations of continuum materials with DEM (12). This section introduces the main aspects of the numerical models used in *GranOO*. In addition, the developments specifically addressed for the presented study are highlighted : the thermal expansion and an improvement of the failure criterion.

<sup>1</sup>see [www.granoo.org](http://www.granoo.org)

#### 4.1. Overview of the numerical procedure

Figure 4 shows the main simulation steps implemented in this study. The first step consists in calibrating the thermo-mechanical parameters of the discrete element model. These microscopic parameters, related to the scale of the discrete elements, are denoted by the  $\mu$  indice. These parameters are the microscopic Young's modulus  $E_\mu$ , radius ratio  $R_\mu$ , tensile strength  $\sigma_{\mu_f}$  and CTE  $\alpha_\mu$ . Considering the values reported in Table 1, both borosilicate glass and alumina parameters are calibrated separately. Readers may refer to the sections 4.4, 4.5 and 4.6 to get more details about the signification of these microscopic parameters and the related calibration method.

After building the initial cubic discrete domains, the second step consists in inserting the spherical alumina inclusions. This step involves a simple geometrical algorithm that is not described here.

The aim of this work is to study the influence of the cracks that happen during the cooling stage of the sample preparation. This stage concerns the range of temperature [450°C - 20°C] from the glass transition temperature to room temperature.

Finally, the damaged virtual samples given by the last step are frozen. In this case, only the elastic behavior is taking into account. To forbid the crack extension, the tensile strength is set to an infinite value. These frozen samples are submitted to virtual tensile tests (see sections 5.1 and 5.2) to evaluate their apparent Young's moduli  $E_M$ .

##### 4.1.1. Synopsis of the main assumptions

In the following discrete element model the main assumptions are :

- the temperature is considered as constant in the whole domain, the heat transfer is neglected because the studied experimental samples are submitted to a very low thermal loading variation.
- the contacts between the discrete elements are not taking into account, the proposed model is a lattice discrete element model. However, the proposed model must be compatible with discrete element model that manages contacts.
- due to the positive CTE mismatch, only the crack opening is considered. In a first approach, the crack closure is supposed insignificant and is not taken into account.

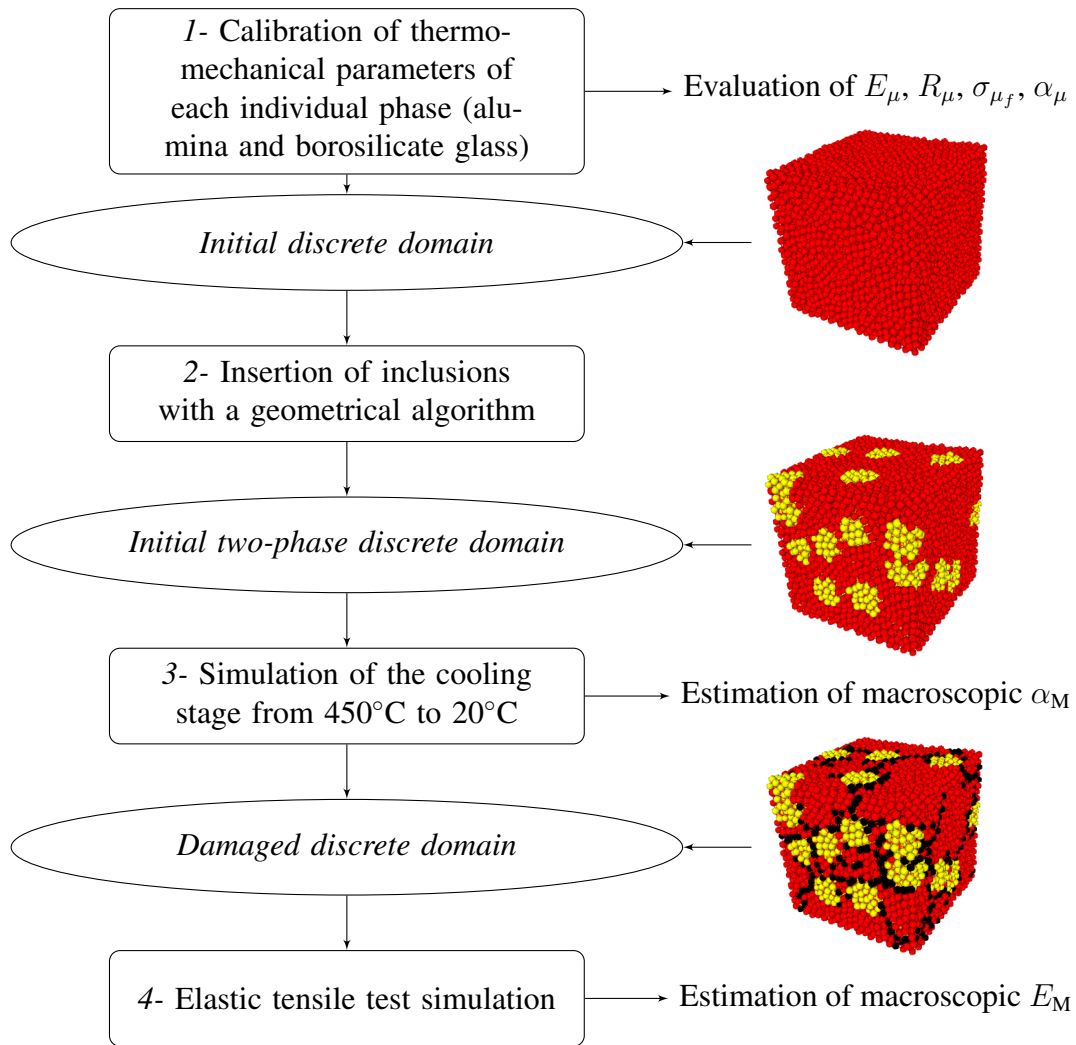


Figure 4: General view of the whole simulation steps

- a crack occurs locally only in a tensile mode. The failure in compression is not allowed locally at the discrete element scale.
- the slight variation of the Young's modulus in respect with the temperature is not considered.

#### 4.2. The explicit temporal scheme

The temporal differential equation is solving by using an explicit integration scheme that is well suited to massive DEM simulations (13) and high velocity phenomena. The velocity Verlet scheme is chosen for its simplicity and efficiency. The discrete element orientations are described by quaternions. Quaternions provide an efficient way to compute discrete element attitudes (14, §2.5). Quaternions must be normalized for every time step to prevent numerical drift. A pure numerical damping factor may be introduced in the numerical scheme as described by Tchamwa and Wielgosz (15) to increase the convergence rate toward static solutions.

To avoid divergence of the temporal scheme, the chosen time step  $\Delta t$  must be lower than the smaller oscillation period  $t_{os}$  of the whole system. For an elastic interaction the period is computed as:

$$\Delta t = \frac{1}{k} \min(t_{os}) \quad \text{with } k \geq 2\pi \quad \text{and } t_{os} = \sqrt{\frac{M_{ij}}{K_{ij}}} \quad (10)$$

where  $M_{ij}$  and  $K_{ij}$  are respectively the equivalent mass and stiffness of an interaction between a discrete element  $i$  and  $j$ . Cambou in (16) proposes a  $k$  value equal to  $2\pi$ . In this study, the stiffness is related to the cohesive beam interactions (see section 4.4) and is equal to :

$$K_{ij} = \frac{E_\mu S_\mu}{l_\mu} \quad (11)$$

where  $E_\mu$ ,  $S_\mu$  and  $l_\mu$  are respectively the cohesive beam Young's modulus, section and length. The equivalent mass of an interaction between a discrete  $i$  and  $j$  is :

$$M_{ij} = \frac{M_i M_j}{M_i + M_j} \quad (12)$$

where  $M_i$  and  $M_j$  are the mass of the discrete element  $i$  and  $j$ . The time step used in this work is about the nanosecond.

#### 4.3. Initial domain building

In this study, only cubic discrete domains are used. The discrete domains are initially packed. The radius of the discrete elements follows an uniform distribution. The range of the distribution is 25%. This value prevents from creating ordered discrete domains that lead to geometrical anisotropy (17). The algorithm used to pack the initial domain comes from the *GranOO* workbench (18). The packing process involves three main steps:

1. the given boundary shape (a cube) is filled with discrete elements randomly placed in the domain. The filling process goes on as long as free places are found.
2. even if no free place exists, a few number of discrete element are inserted. It induces a high level of inter-penetration. A new equilibrium state is achieved by performing a DEM computation. This second step is repeated while the wanted number of discrete element is not reached.
3. finally, the bond network is constructed thanks to a Delaunay triangulation. The nodes of the Delaunay triangulation are the center of the discrete elements. The edges given by the Delaunay triangulation are used to build the bond network.

#### 4.4. Elastic behavior

The cohesive beam bond model (17) is used here to simulate perfectly elastic media characterized by a Young's modulus and a Poisson's ratio. The bond network given by the initial domain building (see previous section) is replaced by a beam network.

In such model, the discrete elements are bonded by Euler-Bernoulli beams. These beams are able to work in tensile, bending and torsion modes. The interactions resulting from the cohesive beams at the discrete element scale are denoted *microscopic*. They are symbolized by the  $\mu$  suffix. In opposition, the emergent behaviors of the whole assembly network are denoted *macroscopic* (see Figure 5). The macroscopic scale is symbolized by the  $M$  suffix. The macroscopic behavior corresponds to the behavior of the simulated material.

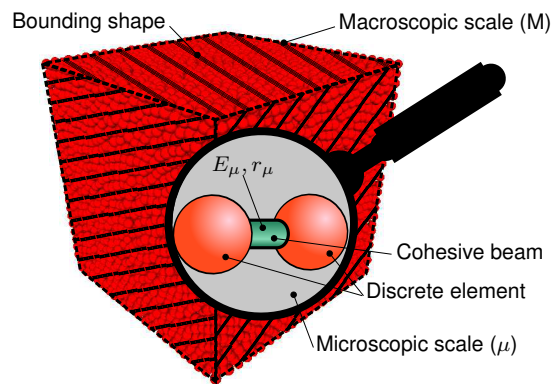


Figure 5: The cohesive beam bond and the two scales involved by the DEM

The cohesive beams are simply defined by two microscopic parameters : a Young's modulus  $E_\mu$  and a radius ratio  $R_\mu$ . The  $E_\mu$  and the  $R_\mu$  values are quantified thanks to a calibration process. The aim of this process is to reach the required values of macroscopic Young's modulus  $E_M$  and Poisson's ratio  $\nu_M$ . The calibration process can be achieved in two main steps :

1. the calibration of the microscopic beam radii in order to merge the imposed value of Poisson's ratio  $\nu_M$  and
2. the calibration of the microscopic beam Young's modulus in order to reach the required value of Young's modulus  $E_M$ .

More details about the calibration process are given in the section 5.3.

#### 4.5. Brittle behavior

Within the discrete element approach, cracks are generally simulated by breaking the cohesive bonds when an imposed criterion is reached (19, 20). The main existing approaches are based on the computation of bond strains (21) or stresses (11). However, these approaches are not able to simulate complex crack paths such as the hertzian cone crack that exhibits on fused silica glass (22). In a previous study, a new criterion, based on the computation of an equivalent Cauchy stress tensor and a maximal hydrostatic pressure value was developed. It has been shown that this criterion gives more accurate results than the standard DEM failure criteria. The equivalent Cauchy stress tensor is computed as :

$$\bar{\bar{\sigma}}_i = \frac{1}{2\Omega_i} \left( \frac{1}{2} \sum_j \mathbf{r}_{ij} \otimes \mathbf{f}_{ij} + \mathbf{f}_{ij} \otimes \mathbf{r}_{ij} \right) \quad (13)$$

where :

- $\otimes$  is the tensor product between two vectors,
- $\bar{\bar{\sigma}}_i$  is the equivalent Cauchy stress tensor of the discrete element  $i$ ,
- $\Omega_i$  is the volume of the discrete element  $i$ ,
- $\mathbf{f}_{ij}$  is the force imposed on the discrete element  $i$  by a cohesive beam that bonds the discrete element  $i$  to another discrete element  $j$  and,
- $\mathbf{r}_{ij}$  is the relative position vector between the center of the two bonded discrete elements  $i$  and  $j$ .

The developed criterion assumes that fracture occurs if the computed tensile hydrostatic stress is higher than a threshold value  $\sigma^f$ :

$$\frac{1}{3}\text{trace}(\bar{\sigma}_i) \geq \sigma^f \quad (14)$$

In the initial study (22), all bonds that belong to the discrete element that reach the  $\sigma^f$  criterion are destroyed. As a consequence, a debonded discrete element occurs and a debris is created. However, the loss of discrete elements when fracture occurs can be viewed as a loss of mass and volume. In the following study, only the half of bonds that belong to the discrete element is destroyed. Hence, a second computation is necessary to select the bonds to break out.

Because brittle failure occurs in tensile mode (mode I), the breaking bond set must follow a surface normal to the higher tensile stress direction. The higher tensile stress direction  $\mathbf{d}_i$  is assumed to be the direction of the vector formed by the principal stress components  $\mathbf{d}_i (\sigma_i^I, \sigma_i^{II}, \sigma_i^{III})$  related to the discrete element  $i$ . The surface ( $S_i$ ) created by the fracture is assumed to be normal to the main principal stresses direction  $\mathbf{d}_i$ . To mimic this surface creation, the bonds between the discrete elements  $i$  and  $j$  are broken assuming the following condition :

$$\mathbf{r}_{ij} \cdot \mathbf{d}_i > 0 \quad (15)$$

where  $\cdot$  is the scalar product and  $\mathbf{r}_{ij}$  is the relative position vector between the bonded discrete  $i$  and  $j$ . This method allows to create a crack path along the surface  $S_i$ . Figure 6 illustrates this process in 2D. The main advantage of this method is to let the possible management of crack closures by taking into account the contacts between unbonded discrete elements. This last aspect (crack closure) is not treated in this study.

#### 4.6. Thermal expansion behavior

All materials subjected to a thermal loading undergo thermal expansion. For a free of crack material, if the temperature is homogeneous in the whole volume, thermal strains do not lead to stress and the mater is still relaxed. As a consequence, imposing forces or torques to discrete elements is not the most valuable way to treat thermal expansion phenomenon using DEM.

The proposed solution consists in incrementing the free length of the cohesive beams  $l_0$  by a  $\Delta l_0$  value computed from the temperature variation  $\Delta T$  (see Figure 7). It leads to the expansion of the whole domain without adding any internal forces. So, free length of cohesive beams become a function of the temperature :

$$l_0(T) = l_0^{\text{initial}} (1 + \Delta T \times \alpha) \quad (16)$$

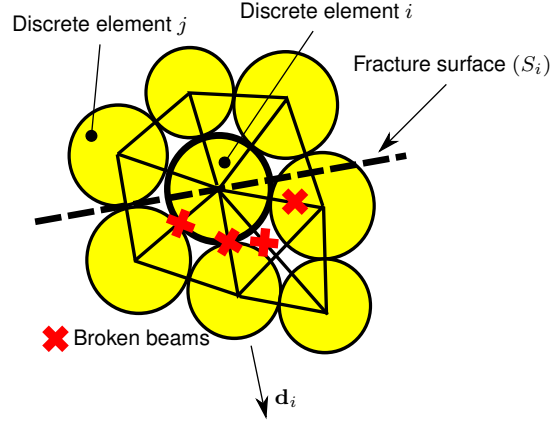


Figure 6: Illustration of the method for selecting broken bonds

where  $\Delta T = T - T_0$  is the temperature variation,  $\alpha$  is the linear thermal expansion coefficient and  $l_0^{\text{initial}}$  is the initial free length for the initial temperature  $T_0$ .

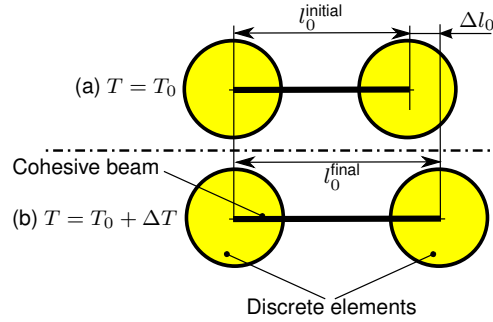


Figure 7: Thermal expansion of the cohesive beams. (a) At the initial temperature  $T_0$ , the free length is  $l_0^{\text{initial}}$ . (b) For a given temperature  $T$ , the free length is  $l_0^{\text{final}} = l_0^{\text{initial}} + \Delta l_0$ .

To avoid confusion, it is important to note that the current lengths  $l$  are not directly affected by these computations. Changing the free length  $l_0$ , for the given cohesive beam, leads to change the reaction forces acting on the bonded discrete elements. If the related discrete elements are unconstrained, the current length  $l$  of the beam converges toward the most updated value of its free length  $l_0$  after a given number of iterations.

#### 4.6.1. Numerical study of thermal expansion

As the other mechanical parameters described in the previous sections, the thermal linear expansion  $\alpha$  is considered at two levels : microscopically ( $\alpha_\mu$ ) and macroscopically ( $\alpha_M$ ). The  $\alpha_\mu$  is the input parameter related to the thermal expansion coefficient of the cohesive beams and the  $\alpha_M$  is the resulting thermal expansion of the bounding shape of the discrete domain.

To study the relation between the microscopic and the macroscopic thermal expansion, some simulations were carried out. The discrete domain used for these simulations is shown in Figure 8. The discrete domain contains around 10,000 discrete elements and the average number of bonds per discrete element is 13.6 (also named coordination number).

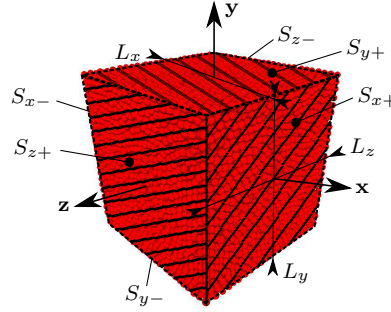


Figure 8: The cubic discrete domain used to study thermal expansion

Thermal expansion is introduced at the microscopic scale by changing the free length of each cohesive beams  $k$  according to equation 16 :

$$l_{0k}(T) = l_{0k}^{\text{initial}} (1 + \Delta T \times \alpha_\mu) \quad (17)$$

In this whole study, the temperature is considered as homogeneous in the material. So, in a first approach, heat conduction is not taken into account.

To measure the macroscopic thermal expansion coefficient  $\alpha_M$ , the length variations of the bounding box are computed and updated during the simulation. This bounding box has six faces :  $S_{x+}$ ,  $S_{x-}$ ,  $S_{y+}$ ,  $S_{y-}$ ,  $S_{z+}$  and  $S_{z-}$ .

In this whole study, the first index 'x', 'y' or 'z' means that the considered surface is normal to the related axis : x, y or z. The second index, minus '-' or plus '+', denotes the location of the face according to the axis direction. For example,  $S_{x+}$  denotes the face normal to the  $x$  axis and located positively along this axis.

The discrete elements that belong to these faces were identified by the preliminary packing algorithm used to build the initial discrete domain (for details about the packing algorithm, see (18), (23) and section 4.3).

The lengths  $L_x$ ,  $L_y$ ,  $L_z$  along the  $x$ ,  $y$  and  $z$  axes of the bounding box are computed by averaging the position vectors of the discrete elements that belong to these faces :

$$L_x = \langle \mathbf{p}_i \cdot \mathbf{x} \rangle_{i \in S_{x+}} - \langle \mathbf{p}_i \cdot \mathbf{x} \rangle_{i \in S_{x-}} \quad (18)$$

$$L_y = \langle \mathbf{p}_i \cdot \mathbf{y} \rangle_{i \in S_{y+}} - \langle \mathbf{p}_i \cdot \mathbf{y} \rangle_{i \in S_{y-}} \quad (19)$$

$$L_z = \langle \mathbf{p}_i \cdot \mathbf{z} \rangle_{i \in S_{z+}} - \langle \mathbf{p}_i \cdot \mathbf{z} \rangle_{i \in S_{z-}} \quad (20)$$

where  $p_i$  is the position vector of the discrete element  $i$ .

According to the equation 16, three macroscopic linear thermal expansion coefficients  $\alpha_{M_x}$ ,  $\alpha_{M_y}$  and  $\alpha_{M_z}$  along the  $x$ ,  $y$  and  $z$  axes are computed as :

$$\alpha_{M_x} = \frac{\Delta L_x}{\Delta T \times L_x^{\text{initial}}} \quad (21)$$

$$\alpha_{M_y} = \frac{\Delta L_y}{\Delta T \times L_y^{\text{initial}}} \quad (22)$$

$$\alpha_{M_z} = \frac{\Delta L_z}{\Delta T \times L_z^{\text{initial}}} \quad (23)$$

where  $\Delta L_x$ ,  $\Delta L_y$ ,  $\Delta L_z$  are the length variation due to thermal expansion of the bounding box.

Figure 9 shows the results of such numerical simulations. The applied thermal loading corresponds to an increase of temperature of 1/20 Kelvin per iteration. The simulation is achieved after 10,000 iteration that corresponds to a total temperature variation of 500 K. The microscopic thermal expansion coefficient used for these simulations is  $\alpha_\mu = 7.6 \cdot 10^{-6} \text{K}^{-1}$ . The evolutions of the macroscopic linear thermal expansion coefficients  $\alpha_{M_x}$ ,  $\alpha_{M_y}$  and  $\alpha_{M_z}$  versus the iterations number are plotted in Figure 9. The given results show that :

1. the evolutions of the three macroscopic linear thermal expansion coefficients  $\alpha_{M_x}$ ,  $\alpha_{M_y}$  and  $\alpha_{M_z}$  are quite similar and
2. the macroscopic thermal expansion coefficients converge toward the value of  $7.6 \cdot 10^{-6} \text{K}^{-1}$  corresponding to the microscopic one.

These two results conduct to :

$$\alpha_\mu = \alpha_{M_x} = \alpha_{M_y} = \alpha_{M_z} = \alpha \quad (24)$$

	$E$ (GPa)	$\nu$	$\sigma_f$ (MPa)	$\alpha$ ( $10^{-6}\text{K}^{-1}$ )
glass	72	0.23	50	11.6
alumina	340	0.24	380	7.6

Table 2: The main thermo-mechanical parameter values of the borosilicate glass and alumina where  $E$  is the Young’s modulus,  $\nu$  is the Poisson’s ratio,  $\sigma_f$  is the failure strength limit and  $\alpha$  is the linear thermal expansion coefficient

The first result ensures that thermal expansion is isotropic and the second result shows that thermal expansion coefficient can be introduced directly without any calibration.

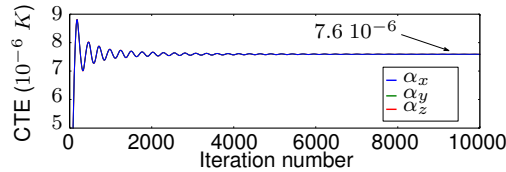


Figure 9: Evolution of the macroscopic linear thermal expansion coefficients  $\alpha_{M_x}$ ,  $\alpha_{M_y}$  and  $\alpha_{M_z}$  versus the number of iterations

## 5. From discrete to continuous quantities

Continuous quantities such as Young’s modulus, Poisson’s ratio, tensile failure strength or coefficient of thermal expansion are computed from discrete quantities. This section focuses on the main methods for computing these quantities.

Because continuous quantities are always considered at the scale of the whole discrete assembly (macroscopic scale), these quantities are not directly computed. Continuous quantities are virtually measured during numerical testings. For instance, mechanical quantities such as Young’s modulus, Poisson’s ratio and tensile failure strength are retrieved through virtual tensile test. The CTE is computed through a virtual thermal expansion test.

A calibration procedure must be achieved to set the microscopic parameter values that match the values of the two simulated constituents : alumina and borosilicate glass. The thermo-mechanical parameter values of these two materials are shown in Table 2.

According to the previous section, the linear thermal expansion coefficient  $\alpha$  has not to be calibrated. However, Young's modulus, Poisson's ratio and failure strength limits have to be calibrated in regard of their microscopic quantities thanks to virtual tensile tests. These virtual tests involve cubic discrete domains similar to the presented one on Figure 8.

### 5.1. Virtual tensile test and computational methods of macroscopic quantities

#### 5.1.1. Imposed displacements

To simulate a tensile test, opposite displacements are imposed to the discrete elements  $S_{x+}$  and  $S_{x-}$ . These displacements are applied along the  $\mathbf{X}$  axis. A small constant velocity of 20 nanometers per iteration is used to apply these displacements.

#### 5.1.2. Numerical measurement of the main normal force $\mathbf{F}$

The cohesive normal forces  $\mathbf{F}_{x-}$  and  $\mathbf{F}_{x+}$  resulting from the imposed displacements are considered as the sum of the local forces  $\mathbf{f}_i$  applied by the beams to the  $S_{x+}$  and  $S_{x-}$  discrete element sets :

$$\mathbf{F}_{x-} = \sum_{i \in S_{x-}} \mathbf{f}_i \cdot \mathbf{x} \quad (25)$$

$$\mathbf{F}_{x+} = \sum_{i \in S_{x+}} \mathbf{f}_i \cdot \mathbf{x} \quad (26)$$

If no failure occurs during the simulation, the cohesive normal forces  $\mathbf{F}_{x-}$  and  $\mathbf{F}_{x+}$  are opposite :

$$\mathbf{F}_{x-} \approx -\mathbf{F}_{x+} \quad (27)$$

The cohesive normal force  $\mathbf{F}$  is computed by averaging the two opposite forces :

$$\mathbf{F} = \frac{1}{2} (\mathbf{F}_{x-} - \mathbf{F}_{x+}) \quad (28)$$

#### 5.1.3. Numerical measurement of the main normal stress $\sigma_{M_{xx}}$

The main normal stress  $\sigma_{M_{xx}}$  is simply computed as :

$$\sigma_{M_{xx}} = \frac{\mathbf{F} \cdot \mathbf{x}}{L_y \times L_z} \quad (29)$$

where  $L_y$  and  $L_z$  are the lengths of the sample along the y and z axes.

#### 5.1.4. Numerical measurement of the main strains

The macroscopic strain  $\varepsilon_{M_{xx}}$ ,  $\varepsilon_{M_{yy}}$  and  $\varepsilon_{M_{zz}}$  along the  $x$ ,  $y$  and  $z$  axes can be expressed as :

$$\varepsilon_{M_{xx}} = \frac{\Delta L_x}{L_x} \quad \varepsilon_{M_{yy}} = \frac{\Delta L_y}{L_y} \quad \varepsilon_{M_{zz}} = \frac{\Delta L_z}{L_z} \quad (30)$$

#### 5.1.5. Numerical measurement of the macroscopic Young's modulus

The macroscopic Young's modulus  $E_M$  is computed as :

$$E_M = \frac{\sigma_{M_{xx}}}{\varepsilon_{M_{xx}}} \quad (31)$$

#### 5.1.6. Numerical measurement of the macroscopic Poisson's ratio

The macroscopic Poisson's ratio  $\nu_M$  is computed by averaging the macroscopic Poisson's ratio values along the  $y$  and  $z$  axes as :

$$\nu_{M_y} = -\frac{\varepsilon_{M_{yy}}}{\varepsilon_{M_{xx}}} \quad \nu_{M_z} = -\frac{\varepsilon_{M_{zz}}}{\varepsilon_{M_{xx}}} \quad (32)$$

$$\nu_M = \frac{1}{2} (\nu_{M_y} + \nu_{M_z}) \quad (33)$$

where  $\nu_{M_y} \approx \nu_{M_z}$ .

#### 5.1.7. Numerical measurement of the macroscopic failure stress

The macroscopic failure stress  $\sigma_{M_f}$  is the value of the macroscopic tensile stress  $\sigma_{M_{xx}}$  when the failure occurs. The failure is considered when a sudden decrease of the measured macroscopic tensile stress  $\sigma_M$  appears (see Figure 10-(c)).

### 5.2. Typical results from virtual tensile tests

Typical behaviors resulting from virtual tensile tests are reported on Figure 10. The (a) and (b) graphs show that the macroscopic Poisson's ratio  $\nu_M$  and the macroscopic Young's modulus  $E_M$  quickly converge towards constant values : 0.23 and 72 GPa respectively . These converged values are considered as the material properties of the domain in regard of their microscopic quantities. The (c) graph shows the evolution of the macroscopic tensile stress  $\sigma_{M_{xx}}$  versus the macroscopic strain  $\varepsilon_{M_{xx}}$ . A sudden decreasing of the  $\sigma_{M_{xx}}$  indicates the failure of the virtual specimen. The corresponding value of  $\sigma_{M_{xx}}$  is considered as the material strength limit  $\sigma_{M_f}$ .

The results plotted in Figure 10 correspond to the macroscopic properties of the glass matrix. In other words, the microscopic parameters were calibrated to match the glass values.

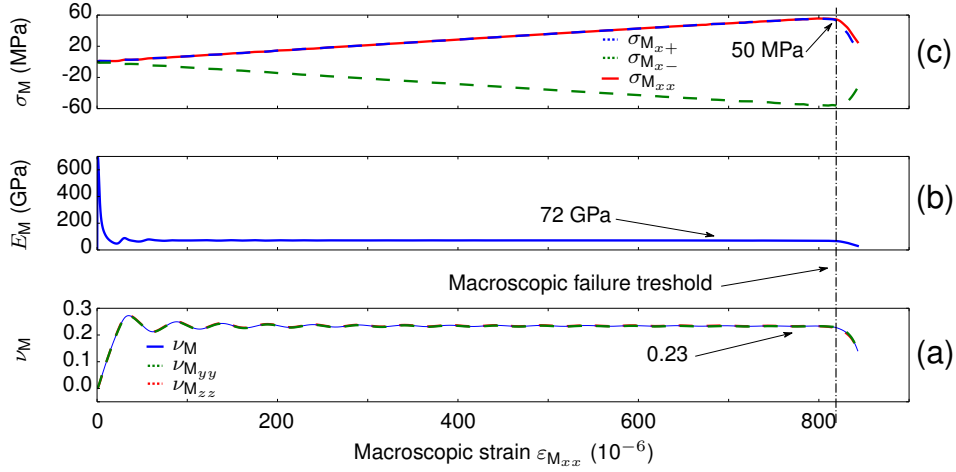


Figure 10: Evolution of (a) the macroscopic Poisson's ratio  $\nu_M$ , (b) the macroscopic Young's modulus  $E_M$  and (c) the macroscopic tensile stresses  $\sigma_M$  versus the macroscopic strain  $\varepsilon_{M,xx}$  during a virtual tensile test

### 5.3. Calibration procedure

Deducing microscopic parameters values that match wanted values at the macroscopic scale presents some difficulties. This problem has been discussed in detail by Ostoja-Starzewski (24). The author proposes micro-macro analytic laws for typical ordered lattice configurations. In the last paragraph (§ 6.3) dedicated to the periodic random lattice network, Ostoja-Starzewski proposes numerical tests to calibrate the model. By the way, analytic approaches are limited to ordered configurations as mentioned by Potyondy and Cundall in (11, §3.1).

Another difficulty is the relationship between the sample topology (shape, refinement, etc.) and emergent macroscopic behaviors. It induces that the microscopic parameters are only valid for a single and unique discrete element sample. This problem was underlined by Hentz et al. in (25) and Liao et al. in (26).

A solution was proposed by Andre and al. in (17) and (22). These studies show that the initial packing processes of the discrete samples is of high level of importance. The packing processes must ensure a stable level of geometrical isotropy, volumic fraction and coordination number between the different created samples. These criteria allows to minimize the level of dependency between the sample topology and the emergent behaviors of these samples. The *Cooker* program, proposed by the *GranOO* discrete element workbench, is able to control these packing parameters.

To minimize the number of simulations, the calibration involves a well defined procedural approach described in (17) and (22). The resulting set of microscopic parameters is independent of the size, the shape or the refinement of the discrete domain. It means that this set of microscopic values can be applied to any kind of discrete domains with arbitrary shapes. Figure 11 shows the convergence rate of the macroscopic Young's modulus  $E_M$ , the macroscopic Poisson's ratio  $\nu_M$  and the macroscopic tensile strength  $\sigma_{fM}$  versus the number of discrete elements. The computations were conducted on discrete samples with an increasing number of discrete element from 2,000 to 20,000 (see Figure 12). The same set of microscopic parameter values was used for all these different samples. Because the initial packing algorithm involves random procedures, four samples were built for each number of discrete element. It explains the scatters at each given point. These curves underline that the macroscopic quantities converge toward single values. It confirms that a given set of microscopic parameter values gives a single set of macroscopic parameters values for any discrete samples.

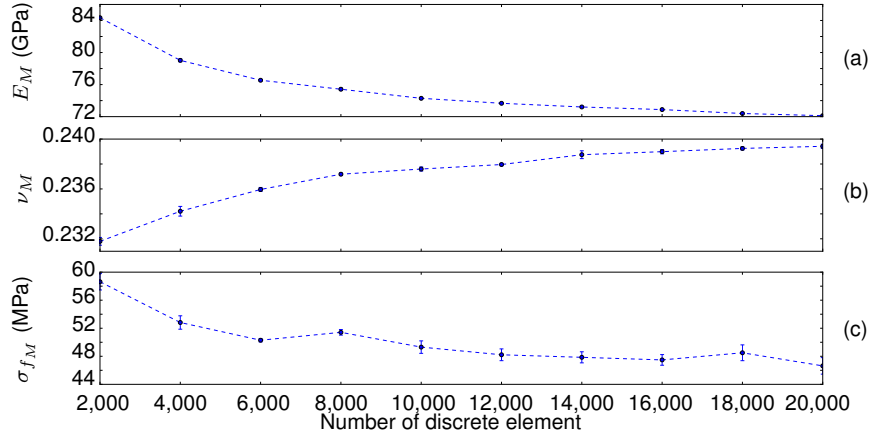
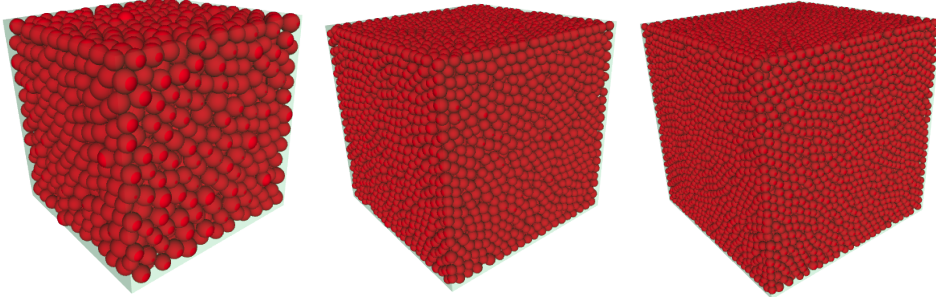


Figure 11: Evolution of (a) the macroscopic (a) Young's modulus  $E_M$ , (b) the macroscopic Poisson's ratio  $\nu_M$  and (c) the macroscopic tensile strength  $\sigma_{fM}$  versus the number of the discrete element

Table 3 sums up the microscopic values of the glass and alumina materials given by the calibration process.



(a) 2,000 discrete elements (b) 10,000 discrete elements (c) 20,000 discrete elements

Figure 12: Snapshot of discrete samples with increasing refinement

	$E_\mu$ (GPa)	$R_\mu$	$\sigma_{\mu_f}$ (MPa)	$\alpha_\mu$ ( $10^{-6}\text{K}^{-1}$ )
glass	5,200	0.1	60	11.6
alumina	24,560	0.1	360	7.6

Table 3: The main microscopic thermo-elastic parameter values of glass and alumina after calibration process where  $E_\mu$  is microscopic Young's modulus,  $R_\mu$  is microscopic radius ratio,  $\sigma_{\mu_f}$  is microscopic failure strength limit and  $\alpha_\mu$  is microscopic linear thermal expansion coefficient

## 6. Two-phase materials

The discrete domains used to obtain the virtual two-phase materials were built in a box shape with approximatively 10,000 discrete elements. Four discrete domains were built to ensure the statistical representativeness of the calculus. After building the discrete domains, a second phase (inclusions) is generated thanks to a geometrical algorithm that randomly distributes spherical inclusions inside the cubic domains. If the inclusions intersect the boundaries of the domains, they are cut by the boundary plane of the cubic domain (see Figure 13a).

For each specimen, several volume proportions of inclusions have been chosen : 0%, 5%, 10%, 15%, 20%, 25%, 30%, 35%, 40% and 45%. The average inclusion radius is  $250 \mu\text{m} \pm 10\%$ . The number of discrete elements that belongs to an inclusion is about 200. The virtual cubic two-phase domains with approximatively 2.2 millimeters length are composed of three types of bonds (see Figure 13b): matrix, inclusion and interface bonds. Because no interphase exists between alumina inclusion and glass matrix (see section 1), the bonds that link a *matrix* discrete element and an *inclusion* discrete element are considered as matrix bonds.

The lengths of the virtual domains were chosen to reproduce a statically rep-

representative sample. The imposed number of discrete elements (around 10,000) corresponds to a good compromise between the precision of the results and the computational time cost.

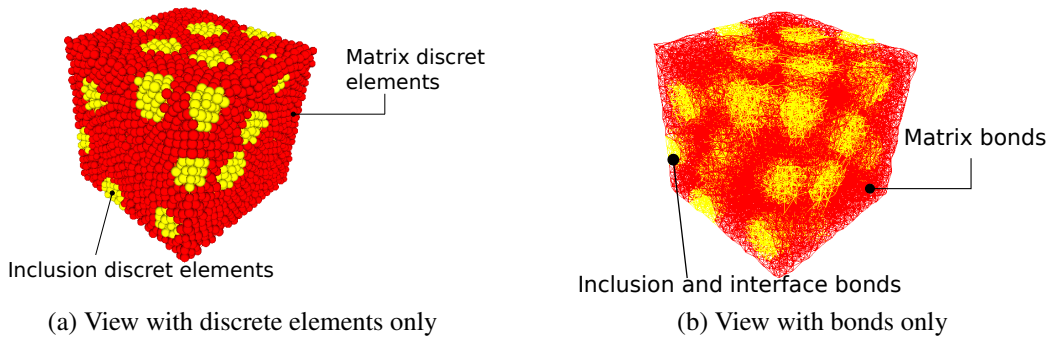


Figure 13: Virtual sample of the two-phase model material

### 6.1. Unbreakable numerical model

As a preliminary approach, the failure stress of each phase is set to an infinite value. So, no micro-crack appears during thermo-elastic numerical test. The domains are submitted to a numerical cooling from 450 to 20°C to get the CTE of virtual undamaged two-phase domains. Then, tensile tests are performed to measure macroscopic Young's modulus. The results in Figure 14 show that the thermo-mechanical behavior of the simulated cohesive two-phase material are consistent with the predictions of H&S model. It allows to validate the numerical two-phase model. However, the experimental results reported in Figure 3 show that this approach is limited to perfect materials.

### 6.2. Breakable numerical model

In this section, the matrix bonds are considered as breakable. Following the approach described in Figure 4, the discrete domains are subjected to cooling tests (where micro-cracks appear), and then, to a tensile test. Here, the virtual tensile tests are non-destructive. The micro-cracks are "frozen" and they are not allowed to propagate themselves during the tensile test. It allows to measure the apparent Young's modulus of the damaged virtual samples. Experimentally, the Young's modulus is measured by ultrasonic pulse echography technique does not provide any additional damage in normal conditions of using (27). The CTE is measured with a standard dilatometer equipment.

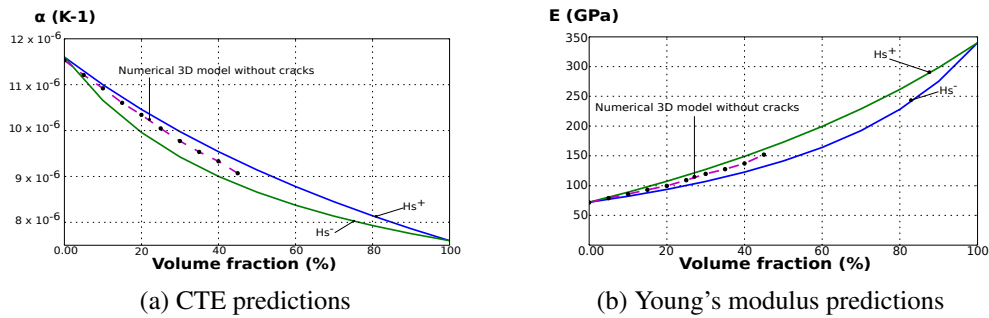


Figure 14: Comparison between numerical and analytical H&S models of free of damage two-phase materials

The numerical results and the experimental observations are plotted on Figure 15. The results of micro-cracked virtual model materials exhibit a highly different behavior than H&S predictions and seem in good agreement with the experimental observations.

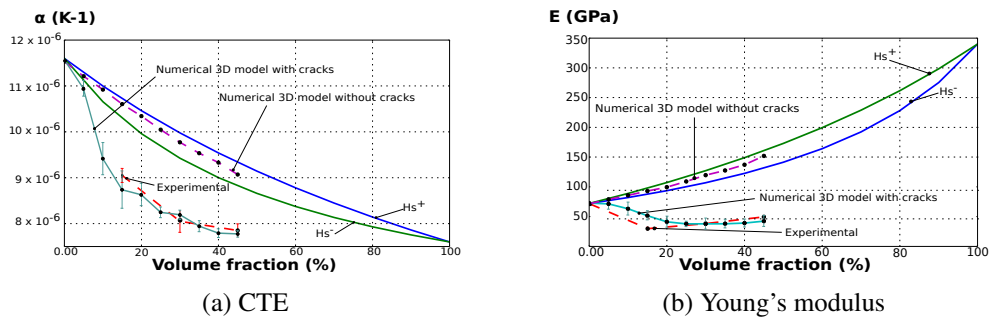


Figure 15: Comparison between numerical predictions and experimental values of damaged two-phase materials

## 7. Discussion

Qualitatively, the evolution of numerical Young's modulus with the increase of volume fraction of inclusions follows experimental observations and remains below H&S predictions. Quantitatively, the numerical results overestimate Young's modulus when volume fraction is lower than 20%. However, Young's modulus estimation is in good accordance with experimental data for volume fraction higher than 20%.

In addition, the numerical prediction of CTE matches quantitatively the experimental observations. For numerical samples, the CTE are measured indirectly from length variations. Figure 16 shows the evolution of numerical and experimental thermal strains versus temperature during a cooling stage from 450°C to 50°C. These data concern an experimental sample and a numerical sample with 45 vol% of inclusions. Figure 16 shows that the numerical results are in good accordance with the experimental observation. The evolution of numerical strains follow two distinct zones named *undamaged* and *damaged*. From this observation, two CTE can be computed from linear regressions applied inside the *damaged* and *undamaged* data range. It is observed that the *undamaged* CTE is inside the H&S bounds. The *damaged* CTE is lower than the lower H&S bound and is very close to the experimental one. Another value of interest is the number of broken beams during a simulation. Figure 16 shows that the strain slope changing corresponds to the beginning of cracking.

This two distinct regimes are not clearly observed on experimental data. This difference is due to the initial level of damage between the experimental sample and the numerical one. At the initial temperature, i.e, 450°C, the numerical sample is free of damage. Therefore, the experimental sample is already slightly damaged. So the changing strain slope is smoothed and not clearly visible. That's why the experimental CTE values reported in figure 15a are deduced from linear regression on the complete range from (450°C to 20°C) while the numerical CTE are deduced from the range 300°C to 20°C.

In addition, only the radial micro-cracks are taken into account in the numerical model. However, real microstructure of such two-phase materials include other discontinuous phenomena, such as debonding around inclusions or defects that may influence the thermo-elastic properties.

As explained in section 2, the system  $\Delta\alpha > 0$  promotes the radial micro-cracks. The agreement between experimental and numerical results while the presence of alumina inclusions increases seems to validate that radial micro-cracks are predominant. For a low volume fraction, the number of radial micro-cracks is low. As a consequence, the other types of damages such as debonding or defects may have a non negligible effects on the apparent Young's modulus.

Radial micro-cracking phenomenon seems to monitor elastic behavior of two-phase model materials for high level of inclusions. So, according to the results in Figure 15, the numerical model may be relevant for quantitative studies. The developed model seems to catch and predict the main phenomena that drives the evolution of Young's modulus and CTE of two-phase damaged materials.

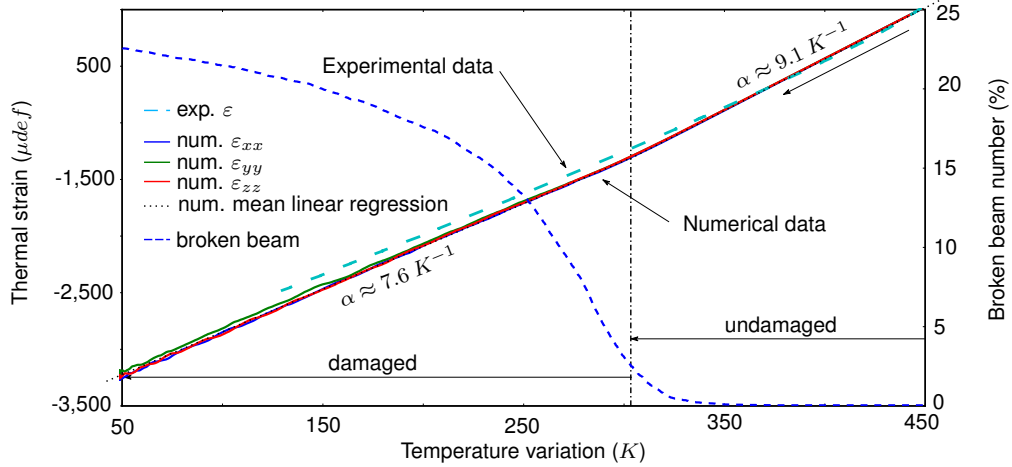


Figure 16: Evolution of (i) numerical and experimental thermal strains and (ii) number of broken beams versus temperature for a sample with 45% of inclusions

## 8. Perspectives and conclusions

This work related to the simulation of thermo-elastic behaviour using DEM presents a significant improvement for discrete element methods applied to the simulation of continuum media. The proposed DEM model has been first validated in regards with well established analytic solutions. In the case of undamaged materials, the numerical results show a good level of accordance with H&S prediction. In addition, the developed method allows to predict (i) the damage level generated by thermal cycle on materials that exhibit a thermal expansion mismatch and (ii) the apparent thermo-mechanical parameters such as Young's modulus and CTE. This study confirms that thermal damages provoke a great influence on apparent thermo-mechanical parameters and the developed model may be applied to a large class of heterogeneous brittle materials : geo-materials, civil engineering materials and ceramics.

The prediction of apparent thermo-mechanical parameters such as Young's modulus, Poisson's ratio or CTE is of high level of importance for engineering applications. The proposed method seems to be adapted to predict this parameters and allows to consider further studies to improve the understanding of industrial multiphase materials. Further investigations may address micro-cracks closure, inclusion debonding or self-healing (that appears when the temperature is greater than the glass transition temperature). The main perspective of this study is the

prediction of apparent thermo-mechanical parameters as a function of (i) thermal history of the material and (ii) the composition of the material. These predictions may help scientists to develop new innovative materials with controlled microstructures.

- [1] Z. Hashin, S. Shtrikman, A variational approach to the theory of the elastic behaviour of multiphase materials, *Journal of the Mechanics and Physics of Solids* 11 (2) (1963) 127–140.
- [2] N. Tessier-Doyen, J. Glandus, M. Huger, Untypical young's modulus evolution of model refractories at high temperature, *Journal of the European Ceramic Society* 26 (3) (2006) 289–295.
- [3] Y. Joliff, J. Absi, M. Huger, J. Glandus, Experimental and numerical study of the room temperature elastic modulus of model materials with partly bonded matrix/particles interfaces, *Computational materials science* 39 (2) (2007) 267–273.
- [4] I. Babuška, B. Andersson, B. Guo, J. Melenk, H. S. Oh, Finite element method for solving problems with singular solutions, *Journal of computational and applied mathematics* 74 (1) (1996) 51–70.
- [5] S. Hentz, F. V. Donzé, L. Daudeville, Discrete element modelling of concrete submitted to dynamic loading at high strain rates, *Computers & Structures* 82 (29-30) (2004) 2509–2524. doi:10.1016/j.compstruc.2004.05.016.
- [6] A. Bobet, A. Fakhimi, S. Johnson, J. Morris, F. Tonon, M. R. Yeung, Numerical models in discontinuous media: Review of advances for rock mechanics applications, *Journal of Geotechnical and Geoenvironmental Engineering* 135 (11) (2009) 1547–1561. doi:10.1061/(ASCE)GT.1943-5606.0000133.
- [7] Y. Tan, D. Yang, Y. Sheng, Discrete element method (dem) modeling of fracture and damage in the machining process of polycrystalline sic, *Journal of the European Ceramic Society* 29 (6) (2009) 1029–1037. doi:10.1016/j.jeurceramsoc.2008.07.060.
- [8] J. SELSING, Internal stresses in ceramics, *Journal of the American Ceramic Society* 44 (8) (1961) 419–419. doi:10.1111/j.1151-2916.1961.tb15475.x.
- [9] P. A. Cundall, O. D. L. Strack, A discrete numerical model for granular assemblies, *Geotechnique* 29 (1979) 47–65. doi:10.1680/geot.1979.29.1.47.

- [10] E. Schlangen, J. G. M. van Mier, Experimental and numerical analysis of micromechanisms of fracture of cement-based composites, *Cement and Concrete Composites* 14 (2) (1992) 105–118, special Issue on Micromechanics of Failure in Cementitious Composites. doi:DOI: 10.1016/0958-9465(92)90004-F.
- [11] D. Potyondy, P. A. Cundall, A bonded-particle model for rock, *International Journal of Rock Mechanics and Mining Sciences* 41 (8) (2004) 1329–1364, rock Mechanics Results from the Underground Research Laboratory, Canada. doi:DOI: 10.1016/j.ijrmms.2004.09.011.
- [12] D. Andre, J. Charles, I. Iordanoff, *3D Discrete Element Workbench for Highly Dynamic Thermo-mechanical Analysis: Gran00*, Wiley, 2015.
- [13] E. Rougier, A. Munjiza, N. W. M. John, Numerical comparison of some explicit time integration schemes used in dem, fem/dem and molecular dynamics, *International Journal for Numerical Methods in Engineering* 61 (6) (2004) 856–879. doi:10.1002/nme.1092.
- [14] T. Pöschel, T. Schwager, *Computational granular dynamics*, Springer, 2005.
- [15] L. Mahéo, V. Grolleau, G. Rio, Damping efficiency of the tchamwielgosz explicit dissipative scheme under instantaneous loading conditions, *Comptes Rendus Mécanique* 337 (11-12) (2009) 722–732. doi:doi:10.1016/j.crme.2009.10.005.
- [16] B. Cambou, M. Jean, F. Radjai, *Micromechanics of Granular Materials*, Wiley, 2009.
- [17] D. André, I. Iordanoff, J. luc Charles, J. Néauport, Discrete element method to simulate continuous material by using the cohesive beam model, *Computer Methods in Applied Mechanics and Engineering* 213–216 (0) (2012) 113 – 125. doi:10.1016/j.cma.2011.12.002.
- [18] M. Jebahi, D. André, I. Terreros, I. Iordanoff, *Discrete Element Method to Model 3D Continuous Materials*, Wiley, 2015.
- [19] F. A. Tavaréz, M. E. Plesha, Discrete element method for modelling solid and particulate materials, *International Journal for Numerical Methods in Engineering* 70 (2007) 379–404. doi:10.1002/nme.1881.

- [20] W. Shiu, F. V. Donze, L. Daudeville, Discrete element modelling of missile impacts on a reinforced concrete target, *International Journal of Computer Applications in Technology* 34 (1) (2009) 33–41. doi:doi:10.1504/IJCAT.2009.022700.
- [21] H. A. Carmona, F. K. Wittel, F. Kun, H. J. Herrmann, Fragmentation processes in impact of spheres, *Physical Review* 77 (5) (2008) 051302. doi:10.1103/PhysRevE.77.051302.
- [22] D. André, M. Jebahi, I. Iordanoff, J. luc Charles, J. Néauport, Using the discrete element method to simulate brittle fracture in the indentation of a silica glass with a blunt indenter, *Computer Methods in Applied Mechanics and Engineering* 265 (0) (2013) 136 – 147. doi:http://dx.doi.org/10.1016/j.cma.2013.06.008.
- [23] D. André, J.-L. Charles, I. Iordanoff, 3D Discrete Element Workbench for Highly Dynamic Thermo-mechanical Analysis: GranOO, Wiley, 2015.
- [24] M. Ostoja-Starzewski, Lattice models in micromechanics, *Applied Mechanics Reviews* 55 (2002) 35–60. doi:10.1115/1.1432990.
- [25] S. Hentz, L. Daudeville, F. V. Donzé, Identification and validation of a discrete element model for concrete, *Journal of Engineering Mechanics* 130 (6) (2004) 709–719. doi:10.1061/(ASCE)0733-9399(2004)130:6(709).
- [26] C.-L. Liao, T.-P. Chang, D.-H. Young, C. S. Chang, Stress-strain relationship for granular materials based on the hypothesis of best fit, *International Journal of Solids and Structures* 34 (31-32) (1997) 4087–4100. doi:10.1016/S0020-7683(97)00015-2.
- [27] M. Huger, D. Fargeot, C. Gault, High-temperature measurement of ultrasonic wave velocity in refractory materials, *High Temperatures. High Pressures* 34 (2) (2002) 193–201.